



HAL
open science

Simultaneous Monitoring of Structural Changes and Phase Distribution of LiFePO₄ Along the Cathode Thickness of Li Metal Polymer Battery

Maria Valeria Blanco, Didier Devaux, Anna-Maija Valtavirta, Carlos Cosculluela, Yves Watier, Lucille Quazuguel, Marc Deschamps, Margaud Lecuyer, Renaud Bouchet, Federico Cova

► **To cite this version:**

Maria Valeria Blanco, Didier Devaux, Anna-Maija Valtavirta, Carlos Cosculluela, Yves Watier, et al.. Simultaneous Monitoring of Structural Changes and Phase Distribution of LiFePO₄ Along the Cathode Thickness of Li Metal Polymer Battery. *Journal of The Electrochemical Society*, 2020, 167 (16), pp.160517. 10.1149/1945-7111/abcd4d . hal-03248162

HAL Id: hal-03248162

<https://hal.science/hal-03248162>

Submitted on 3 Jun 2021

HAL is a multi-disciplinary open access archive for the deposit and dissemination of scientific research documents, whether they are published or not. The documents may come from teaching and research institutions in France or abroad, or from public or private research centers.

L'archive ouverte pluridisciplinaire **HAL**, est destinée au dépôt et à la diffusion de documents scientifiques de niveau recherche, publiés ou non, émanant des établissements d'enseignement et de recherche français ou étrangers, des laboratoires publics ou privés.

Simultaneous Monitoring of Structural Changes and Phase Distribution of LiFePO₄ Along the Cathode Thickness of Li Metal Polymer Battery

Maria Valeria Blanco^{1,z}, Didier Devaux^{2,*z}, Anna-Maija Valtavirta^{3,4,5}, Carlos Cosculluela¹, Yves Watier¹, Lucille Quazuguel², Marc Deschamps⁶, Margaud Lecuyer⁶, Renaud Bouchet^{2,*} and Federico Cova¹

¹ European Synchrotron Radiation Facility, 71 Avenue des Martyrs, 38000 Grenoble, France.

² Univ. Grenoble Alpes, Univ. Savoie Mont Blanc, CNRS, Grenoble INP*, LEPMI, 38000 Grenoble, France.

*Institute of Engineering and Management Univ. Grenoble Alpes.

³ Department of Applied Physics, Aalto University, P.O. Box 11100, FI-00076 Aalto, Finland.

⁴ Department of Physics, University of Helsinki, P.O. Box 64, FI-00014, University of Helsinki, Finland.

⁵ Helsinki Institute of Physics, Helsinki, Finland.

⁶ Blue Solutions, Odet, Ergué Gaberic, 29500 Quimper, France.

^zE-mail: maria.v.blanco@ntnu.no, didier.devaux@grenoble-inp.fr

* Electrochemical Society Active Member

Abstract

Probing the structural changes that electrode materials undergo during electrochemical cycling while monitoring their spatial distribution within the volume gives valuable insights on dynamic processes, *i.e.* side reactions and evolution of phase migration barriers, often associated to capacity and power limitation. In this work, we present an electrochemical cell to perform spatial and time resolved *operando* synchrotron X-ray diffraction on Lithium (Li) metal polymer batteries operating at 80 °C. A 3.2 mm diameter battery made of a Li metal anode, a LiFePO₄ based cathode, and a solid polymer electrolyte acting as separator, is placed

inside a glass-based casing and cycled at a beamline. The cylindrical cell geometry with its small size enables to follow the phase transformations occurring at different states of charge and at different cathode heights. It is possible to create spatially resolved phase distribution plots and to differentiate active material structural changes occurring close to the interface with the electrolyte from those at the current collector vicinity. The results provide a direct observation of the Li diffusion in the LiFePO_4 and FePO_4 phase distribution. In addition, synchrotron X-ray diffraction computed tomography (XRD-CT) measurements were performed to obtain phase distribution maps at different heights of the battery assembly.

Introduction

Lithium (Li) based batteries lead the market of power electronic devices, hybrid and full electric vehicles, and are a promising solution for storing and releasing the energy generated by stationary applications, such as solar panels and wind turbines^{1,2}. In order to meet the demands required for the above-mentioned applications, the development of improved high-energy and high-power density electrode materials with stable reversible capacities after prolonged cycling is essential.

The design and engineering of electroactive materials requires a comprehensive understanding of the complex interplay between their structural properties and their electrochemical performance in a cathode³. Indeed, it is known that the occurrence of incomplete or secondary (parasitic) reactions within an electrode, either due to phase migration barriers, phase segregation or merely local limitations in the electronic and ionic transport, can severely affect the redox properties and cycle life of the active materials⁴⁻⁶. Thus, the sole study of their structural evolution upon charge and discharge is not sufficient to fully interpret the electrochemical performance of battery systems and *operando* analysis is needed to identify processes leading to capacity and power fade.

An interesting example is LiFePO_4 , which has been intensively studied due to its great performance as cathode of Li-based batteries^{7,8}. Numerous structural studies have shown that at low de(lithiation) rates LiFePO_4 (LFP) transforms to FePO_4 (FP) through a first-order transition. In addition, it was recently reported that at high de(lithiation) rates the first order phase transformation is suppressed and LFP transitions to FP via solid solution reaction^{9,10}. In either case, the phase boundary propagation plays an important role in the de(lithiation) kinetics. In view of this, many reports have focused in the study of the two-phase boundary evolution upon electrochemical de(lithiation) through different experimental¹¹⁻¹³ and theoretical approaches^{14,15}. However, even for well-studied active materials, such as LFP, few reports have tracked the dynamics of the spatial distribution of redox reaction products within the electrode upon electrochemical cycling¹⁶⁻¹⁸. This information allows detecting nonuniform chemical processes and identifying local domains of unreacted material, which is crucial for the development of thick electrodes with enhanced specific energy densities and for optimizing rate-dependent battery performance.

Operando synchrotron X-ray diffraction (XRD) measurements allow to obtain structural information of the battery components in times shorter than a second, which makes it a powerful tool to track in real time phase transformations and structural changes on the anode and cathode, and relate them to the battery electrochemical performance¹⁹⁻²². *Operando* XRD experiments on battery systems are usually performed on modified coin cells²³, pouch cells^{24,25} and the so-called "Swagelok" cells^{26,27} using a transmission geometry. In the standard configuration of these cells, the X-ray beam is parallel to the electrode stack axis and the diffracted signal contains contributions from the two electrodes, the separator, the current collector, the electrolyte and the casing. However, in the last years novel cell designs have shown the great benefit of using cylindrical cells, in which measurements can be performed in transmission mode with the X-ray beam perpendicular to the electrode stack axis²⁸⁻³³. Such

configuration enables not only to separately obtain structural information of the different components, but also to collect information at different heights within an individual component. This allows to differentiate processes that occur at the interface between the electrode and the electrolyte from those taking place at the interface between the electrode and the current collector. In consequence, *operando* XRD experiments on cylindrical shaped cells permits to finely monitor the evolution of the redox reactions with a spatially resolved approach.

In this work, we present a simple glass-based electrochemical cell suitable for *in situ/operando* synchrotron XRD and XRD computed tomography (XRD-CT) studies. A 3.2 mm diameter Li metal battery comprising LFP composite cathode and a poly(ethylene oxide) based solid polymer electrolyte (SPE) was assembled within the electrochemical cell and cycled at 80 °C. *Operando* synchrotron XRD measurements performed along the electrode height allowed to track in real time the (de)lithiation reactions while visualizing the advance of the reaction front and the phase distribution of LFP and FP. In addition, ex-situ XRD-CT tomography enabled to map the spatial distribution of the different phases at specific heights of the battery and to clearly distinguish the different battery components.

Experimental

Battery assembly

The battery assembly consisted in the superposition of a Li metal anode, a solid polymer electrolyte (SPE) layer, and a composite LiFePO₄ based cathode³⁴. The Li metal of typical thickness $60 \pm 5 \mu\text{m}$ was stored in an Argon filled glovebox (Campus, Jacomex) with sub-ppm values of oxygen and water. The SPE is a random copolymer comprising poly(ethylene oxide) (PEO), to ensure ionic motion, and poly(propylene oxide), to provide flexibility to the resulting membrane. The copolymer was doped with lithium bis-trifluoromethanesulfonimide (LiTFSI)

salt at the concentration required to ensure a molar ratio of ethylene oxide to Li salt (EO:Li) of 25. The copolymer and LiTFSI were dissolved in Dimethylformamide by stirring for several hours in a vial at 80 °C. When the solution was clear and transparent, it was poured onto a Teflon Petri dish and dried at room temperature for 8 h. To remove any traces of solvent the Petri dish was further dried in an oven at 60 °C for three days. The resulting membrane was peeled off the Teflon substrate and transferred to the glovebox for at least a week prior to any further manipulation. The SPE was then cut into pieces, hot pressed at 80 °C and then pressed at 200 bar for several minutes. After pressing and cooling, 18 µm thick SPE disks were punched out.

Cathode composite electrodes using LiFePO₄ active material were prepared by Blue Solutions through an extrusion process. The thickness of the cathode deposited on top of an Al current collector was about 48 µm. Inside the glovebox, a 2 mm diameter Li disk and a 3 mm diameter SPE disk were punched out from the Li foil and the SPE, respectively. Both materials were laminated at 80 °C and 3 bars multiple times using a home-made laminating machine until the SPE was fully adherent to the Li. The electrolyte thickness was checked after the laminating process and no variation was observed. Then, a 3 mm diameter cathode disk was also punched out from the electrode foil and gently pressed onto the SPE. The Li metal polymer battery was obtained after laminating several times the three layers to ensure good adhesion between them. After assembly, the batteries were placed inside the electrochemical cells.

Operando X-ray diffraction

Operando X-ray diffraction measurements were performed at the High Energy X-ray Diffraction Beamline ID31 at the European Synchrotron Radiation Facility (ESRF). **Figure 1** shows a sketch of the experimental configuration.

The electrochemical cells were connected to a SP150 or a SP240 (BioLogic SAS) potentiostat and cycled at 80 °C between 2.75 V and 3.8 V vs. Li⁺/Li. The batteries were

galvanostatically cycled at current density (J) of $0.06 \text{ mA}\cdot\text{cm}^{-2}$ corresponding to a charge and discharge rate of $C/8$. At the end of the galvanostatic charge step, a constant voltage of 3.8 V vs. Li^+/Li was applied for 1 h . In between each charge and discharge step, the cells were subjected to a 18 min resting period in order to relax the concentration gradients. At each step, the charge or discharge capacity were calculated by integration of J over time (t) and converted into fraction x of Li in the Li_xFePO_4 with $0 < x < 1$.

Synchrotron XRD data was collected upon electrochemical cycling using a 70 KeV monochromatic X-ray beam. The detector to sample position was calibrated using a NIST CeO_2 standard. The beam was focused to a spot size of $5 \mu\text{m} \times 20 \mu\text{m}$ vertical \times horizontal ($V \times H$). XRD scans along the principal axis of the battery assembly were performed in steps of $5 \mu\text{m}$, with an acquisition time per frame of 1 s . The electrochemically active portion of the glass-tube cells can be scanned from the bottom of the anode to the top of the cathode current collector in approximately 1 min . Such short acquisition times allows to quickly follow the state of each individual component at similar voltages. The data was collected using Pilatus 2M CdTe plate detector and integrated using pyFAI package³⁵. The XRD patterns were refined by the Rietveld method as implemented in the GSAS II package³⁶.

A custom-made heater was built to perform *operando* XRD measurements at $80 \text{ }^\circ\text{C}$. In order to optimize beamtime usage, the heater was designed to allow the simultaneous operation of two glass cells. Pictures of the experimental setup are displayed in **Figure S1** of the electronic supporting information, and schemes and a detailed description of the heater system are presented in **Figure S2**.

X-ray diffraction computed tomography (XRD-CT)

The glass electrochemical cell was mounted onto a Huber goniometer head. X-ray diffraction computed tomography measurements were performed using 50 translation steps,

with a step size of 60 μm for each translation, covering 0 - 180 degrees angular range. In total 180 angles were probed. A light 10 % trimmed mean filter was applied to remove any outliers. The 2D diffraction image data sets were converted to 1D powder diffraction patterns using the pyFAI software. Entire diffractograms were reconstructed for each voxel of the cell using an in-house developed software adapted from Finegan *et al.*³⁷.

Results and discussion

Electrochemical glass cell

Many of the reported cylindrical electrochemical cells used for *in situ/operando* XRD experiments on battery systems utilize polytetrafluoroethylene (PTFE) or perfluoroalkoxy alkane (PFA) casings. However, these polymers are sensitive to radiation and damage can be observed after prolonged exposure times at high X-ray doses³⁸. Furthermore, they exhibit sharp Bragg reflections within the 2θ range that is of interest for most electrode materials. To diminish the background signal and X-ray absorption of the housing, we developed an electrochemical cell using a borosilicate glass tube as main component. In the case of using electrolytes that might be reactive to glass, a thin Kapton tube can be introduced in between the glass tube and the sample to prevent direct contact between them. Swagelok fittings were used to ensure a proper sealing and airtight conditions in the interior of the cell. The electrochemical cell is designed to use simple and commercial components and can be adapted to different sample sizes by changing the diameter of the main glass tube. Furthermore, it enables the construction of a rack in which several cells can be cycled simultaneously. The possibility of building a high-throughput setup is especially important for large scale facilities applications^{23,27}, where acquisition times are significantly shorter than electrochemical reactions and an efficient use of the allocated beamtime is highly valued.

A picture and a side-view sketch of the glass cell are displayed in **Figure 2a**. The main body of the electrochemical cell is constituted by an 80 mm long borosilicate glass tube of 4 mm outer diameter and 3.3 mm inner diameter. One of the ends of the glass tube is glued to a 1/4" 316L stainless steel VCO O-ring face seal fitting (316L-4-VCO-3A) using an air-tight temperature-resistant epoxy glue, while the other end is glued to a 1/4" to 1/8" stainless steel tube fitting reducer. The VCO fittings were selected with the aim of facilitating an adequate sealing inside the glovebox, while the tube fitting reducer allows the airtight insertion of a metallic piston on the top part of the cell. The battery assembly is placed on top of a stainless-steel shim, which is seated on top of a stainless-steel compression spring. The spring is used to ensure a constant contact pressure of the battery assembly during operation. The current is transmitted through plungers located at both ends of the battery assembly and collected with crocodile clips connected to the potentiostats (see **Figure S1**).

To obtain a direct comparison between the background signal of the proposed glass and that of the standard PTFE Swagelok cells, a PTFE cell of 3.3 mm inner diameter was built using Swagelok straight unions as the main body. The inner and outer parts of the tube were machined in order to ensure a smooth pathway in the interior of the cell and to diminish the thickness of the PTFE wall on the way of the beam. A picture and a side-view sketch of the cell, together with its corresponding X-ray diffraction signal are depicted in **Figure 2b**.

The diffraction signals of the empty glass and PTFE cells are plotted together in **Figure 2b**. The PTFE-based cell exhibits a strong Bragg reflection at $2\theta = 2.07^\circ$ together with several small peaks at 2θ values ranging from 3.5° to 6.5° on top of a very noticeable background signal. In the case of the glass cell, a bump of intensity is observed at $2\theta = 2.49^\circ$, which evidences the amorphous nature of the cell casing.

Operando XRD analysis during charge and discharge

In **Figure 3** is depicted the X-ray diffraction pattern of the battery mounted on the glass cell and heated at 80 °C prior to cycling, *i.e.* discharged. The pattern was collected using a 0.6 mm x 0.6 mm (V x H) beam, in order to capture the contributions from all the battery components. The diffractogram was fitted to the Pmnb LiFePO₄ phase and Im-3m Li cubic phase. The Rietveld refinement results are displayed together with the experimental data, showing very good agreement.

With the aim of visualizing the phase distribution of the primary components along the principal axis of the battery assembly, the beam was focused to a spot size of 5 μm x 20 μm (V x H). Preliminary scans were performed to determine the center position of the cell. The collected XRD patterns are displayed in the waterfall plot of **Figure 4a**. From the plot, two regions can be clearly distinguished. A first one, in which cubic Li is the main phase and a second one in which LFP is dominant. In between the two phases is localized the polymer electrolyte, which is in its molten state at 80 °C and therefore does not show any sharp Bragg reflection.

The main reflections of each phase were fitted to a Gaussian function and peak areas were calculated. The obtained results allowed to create phase distribution plots along the battery assembly height, which are displayed in **Figure 4b**. Both, Li and LFP phases exhibit a symmetrical distribution around central points located at 40 μm and 110 μm of the battery assembly height, respectively. Although the tails of Li and LFP phase distribution plots show a coexistence between both phases in the range from 50 μm to 80 μm of the battery assembly height, the quantity of each component under this condition is below 5 %. This overlap is then attributed to misalignments of the battery components, where either the Li or the LFP layer are tilted with respect to each other. Gaussian fittings of the displayed LFP phase distribution curve

indicate a Full Width at Half Maximum (FWHM) of 47 μm , which shows very good correspondence with the measured cathode thickness of about 48 μm .

After completion of the first scan, showing the initial phase distribution of the primary components, the battery was subjected to a charge-discharge electrochemical cycle. During this process, X-ray measurements along the entire assembly were performed in order to follow the behavior of the battery. **Figure 5a** presents the XRD patterns collected upon charge and discharge at a position of the battery height close to the interface between the cathode and the SPE. The voltage profiles acquired upon charge and discharge are displayed in **Figure 5b**. Each open circle in the charge/discharge plots corresponds to one diffractogram in **Figure 5a**.

A common feature present in all the depicted XRD patterns is a bump of intensity at low 2θ values. This is ascribed to the SPE, which is in its molten state and therefore presents an amorphous signal. Initially, LiFePO_4 is the sole phase present and the characteristic peaks of this phase are only observed. Upon charge, the voltage profile transitions to a plateau, at about 3.45 V vs. Li^+/Li , which is accompanied by a gradual disappearance of the reflections corresponding to LFP. At the same time, the reflections belonging to the FePO_4 (FP) phase emerge and grow. Although the growth of the FP peaks is clearly visible, it can be observed that a portion of the LFP phase remains after completion of the charge step. A post-mortem optical inspection showed that a small portion of the cathode disk was detached from the battery during the assembly and was trapped in between the side of the stack and the glass wall. This piece was not in contact with the rest of the battery and thus remained in its initial state during the entire experiment.

During the subsequent discharge process, the reduction reaction towards the formation of LFP occurs. In this case, the plateau develops at a potential of 3.35 V vs. Li^+/Li , which evidences a significant polarization compared with the charge plateau. Along the discharge plateau, the intensity of FP phase reflections starts to fade, until their complete disappearance.

At the end of the discharge, LFP is again the only phase present. It can be seen from **Figure 5b** that the time needed to reach the lower cut-off potential is shorter than the one required to charge the battery, which evidences a low Coulombic efficiency. It has to be noted that the goal of this study is to show the capability of the electrochemical cell rather than getting high performances through battery assembly optimization.

Phase distribution at different states of charge

The main advantage of the presented glass-tube cell is that it allows to easily probe the electrochemical reaction kinetics throughout the height of the electrodes while monitoring the advancement of the reaction front. This section illustrates the dynamics of LFP and FP phase distributions along the electrode height upon electrochemical cycling. Considering the low *C*-rate used to cycle the battery and the short times required to probe the entire height of the cathode (less than 1 min), it is assumed that the XRD patterns recorded during the experiment are representative of the state of the active materials.

The evolution of the reaction front profile is determined by quantifying the phase percentages of LFP and FP at different cathode heights during cycling. Peak areas of reflections (020) and (200) of LFP and FP, respectively, were fitted to a Gaussian function. Each full circle in **Figure 6a** represents the fitted areas of LFP or FP at a specific electrode height and voltage value. It is important to mention that the selected Bragg reflections of the LFP and the FP phases have different maximum areas, since they belong to different crystallographic groups and thus cannot be compared to each other. In addition, given that the portion of the cathode disk trapped in between the side of the stack and the glass wall did not react during the charge and discharge processes, the intensities belonging to this LFP amount were easily identified and subtracted from the XRD patterns. The inset number shown within each plot (#) in **Figure 6a** is related to the charge and discharge voltage values depicted in **Figure 6b**. As indicated within the plot #11, for example, the Li layer is located at left side of the cathode, while the

current collector at the right side. The LFP phase percentages corresponding to the selected data points are also plotted in **Figure 6b**. Since total phase volume illuminated by the X-ray beam is related to the scattered intensity by a square factor, the plotted LFP phase percentages were estimated by calculating the square root of the ratio between the peak area at that point and the initial LFP peak area.

In **Figure 6a**, plot #0 shows the phase distributions corresponding to the initial state of the battery cell where the only phase present is LFP. LFP is symmetrically distributed around a peak centered at an electrode height of 108 μm . Selected data sets corresponding to the charge plateau, from plot #11 to plot #23, show the gradual decrease of LFP phase and the growth of the FP phase. Plot #11 displays the distribution of FP and LFP phases corresponding to an x value in Li_xFePO_4 of 0.58. At this stage, approximately 50 % of the initial LFP has transitioned to the FP phase (see **Figure 6b**). It can be noticed that the spatial distribution of the newly formed FP phase is shifted towards the interface between the electrode and the SPE, while the active material located at higher electrode heights (*i.e.* closer to the current collector) remains unreacted. As the reaction proceeds, the FP phase becomes more dominant. In the final stages of the charge step (plot #20), when x in Li_xFePO_4 is close to 0.22, the percentage of FP is of approximately 76 % (see **Figure 6b**). The charge reaction is almost completed when x in Li_xFePO_4 reaches 0.06 (plot #23) and only 5 % of the original amount of LFP is present. At this instance, an even distribution of the FP phase across the electrode height is evidenced, and the last residue of LFP phase is located close to the interface with the current collector. After completion of the charge process (plot #26) the only phase present is FP. This propagation of the reaction front starting at the cathode/electrolyte interface and developing until the current collector is similar to that reported by Liu *et al.*³⁹ on a Li-LFP battery comprising a liquid electrolyte at a 50% state of charge using *ex situ* synchrotron X-ray microdiffraction. In addition, using *in situ* energy-dispersive XRD on coin cell, Strobridge *et al.* mapped the

inhomogeneity of the electrochemical reaction in LFP cathodes⁴⁰. The authors shows that on the first cycle, the ionic dynamics are limited by the Li diffusion in the electrolyte and that the LFP oxidation occurs preferentially in areas closer to the separator than to the current collector. A similar conclusion was also drawn by Orikasa *et al.* who performed *ex situ* two dimensional X-ray absorption spectroscopy on LFP based cathode of low porosity.⁴¹ For Li polymer electrolyte batteries the ionic transport in the polymer electrolyte acting as separator and as cathode binder is the rate limiting process³⁴. Thus, during charge the Li⁺ ions produced during the LFP oxidation have to diffuse toward the Li metal anode through the polymer electrolyte domain inducing a need of anion species to compensate locally the excess of cationic charge. This process is thus facilitated at the cathode/SPE interface rather than in the depth of the tortuous cathode leading to a faster overall kinetics at the electrode/electrolyte interface. Similarly, during discharge, the reaction front will also develop from the cathode/electrolyte interface to the current collector due this time to excess of anionic species because of the Li⁺ ion consumption during LFP reduction.

Selected data sets corresponding to the discharge process are depicted from plot #29 to plot # 43. During this galvanostatic step, the phase transformation towards the formation of LFP occurs. At the beginning of the discharge, plot #29, the electrochemical reactions proceed from the SPE/cathode interface. This is still visible at plot #34, where the more prominent amount of LFP phase is clearly shifted towards the left. This behavior can also be explained by the ionic transport limitation through the electrolyte domain within the electrode volume. The phase distribution of FP corresponding to the final state of the discharge (plot #43) shows the presence of a residual amount of FP in the region further away from the interface with the SPE, indicating an incomplete phase transformation. Such inhomogeneous electrochemical processes probed by XRD have a direct correlation with the low Coulombic efficiency evidenced from the voltage profile plots. The proposed glass-tube electrochemical cell permits

thus to quickly probe the phase transformation within electrodes depending on their thicknesses and to determine the location of the failure processes.

X-ray diffraction computed tomography (XRD-CT)

Ex-situ room temperature XRD-CT was used to obtain phase distribution maps of the battery assembly components at different heights. The goal is to prove the effectiveness of the glass-tube cell for different X-ray characterization techniques and to demonstrate the high quality of the reconstructed diffraction patterns.

For each voxel of the reconstructed volume, an XRD pattern representative of the battery at that specific spatial position was obtained. Standard back-projections techniques were used for the reconstruction, and the initial results were corrected to take the surroundings into account as described by Finegan et al.³⁷ **Figure 7a** displays the phase distribution maps of glass, LFP and Li of a slice corresponding to the interface between the cathode and the SPE, which is semi-crystalline at room temperature. The reconstructed XRD patterns of three voxels, located at the edges of the cathode (position #1 electrolyte/electrode interface and position #3 collector/electrode interface) and on its center (position #2), are presented in **Figure 7b**. The high quality exhibited by the obtained patterns allows to perform refinements using the Rietveld method. Interestingly, the reconstructed XRD pattern corresponding to position #2 exhibits the highest signals of the cathode and SPE. According to reflections at $2\theta = 2.31^\circ$ and $2\theta = 3.65^\circ$ the presence of the SPE is not homogeneous through and presents significant variations at the edges. This may be caused by the SPE being trapped in the central part of the battery during the assembly process. **Figure 7a** also evidences the presence of a small amount of Li at the right side of the electrode. This can be caused by a displacement of the Li foil during the preparation of the cell that resulted in part of the Li film being bent at the side of the cell.

Conclusions

A versatile design of an electrochemical cell suitable for *in situ/operando* synchrotron X-ray diffraction characterization of Li batteries is reported. The main body of the cell is a glass tube, which enabled to collect low-background high quality X-ray diffraction data, and the rest of the primary components are commercially available items. The cell was successfully used to perform high temperature time and spatial resolved *operando* synchrotron X-ray diffraction studies and *ex-situ* X-ray diffraction computed tomography analysis on a Li metal battery comprising a LiFePO₄ based cathode and a solid polymer electrolyte, operated at 80 °C.

Operando synchrotron XRD measurements performed along the electrode principal axis allowed to monitor in real-time the structural evolution and phase distribution of the LiFePO₄ and FePO₄ phases within the electrode upon electrochemical cycling. The results allowed to visualize the incipient growth of the FP (resp. LFP in discharge) phase upon charging at the interface between the cathode and the SPE. During the subsequent discharge reaction, the phase transition towards the formation of LFP is also initiated at the interface between the cathode and the SPE. In this case, the diffusion of Li⁺ ions through the newly formed LFP was severely limited and the reaction was not fully completed. The dynamic phase distribution plots revealed that the unreacted portion of the active material was located at the vicinity of the interface between the cathode and the current collector.

The reported results show that *operando* spatial and time-resolved X-ray diffraction studies are essential to fully understand the behavior of electrode materials under working conditions and to get insights in their degradation and failure processes.

Acknowledgement

The authors thank Beamline ID31 of European Synchrotron Radiation Facility for in-house beamtime allocation. We thank Florian Russello and Tiago Couthinio for their help with the preparation of the experimental setup.

References

- (1) Kim, J. G.; Son, B.; Mukherjee, S.; Schuppert, N.; Bates, A.; Kwon, O.; Choi, M. J.; Chung, H. Y.; Park, S. A Review of Lithium and Non-Lithium Based Solid State Batteries. *J. Power Sources* **2015**, *282*, 299–322.
<https://doi.org/10.1016/j.jpowsour.2015.02.054>.
- (2) Kurzweil, P.; Garche, J. 2 - Overview of Batteries for Future Automobiles. In *Lead-Acid Batteries for Future Automobiles*; Garche, J., Karden, E., Moseley, P. T., Rand, D. A. J., Eds.; Elsevier: Amsterdam, 2017; pp 27–96. <https://doi.org/10.1016/B978-0-444-63700-0.00002-7>.
- (3) Meng, J.; Guo, H.; Niu, C.; Zhao, Y.; Xu, L.; Li, Q.; Mai, L. Advances in Structure and Property Optimizations of Battery Electrode Materials. *Joule* **2017**, *1* (3), 522–547. <https://doi.org/10.1016/j.joule.2017.08.001>.
- (4) Jung, S.-K.; Gwon, H.; Hong, J.; Park, K.-Y.; Seo, D.-H.; Kim, H.; Hyun, J.; Yang, W.; Kang, K. Understanding the Degradation Mechanisms of LiNi_{0.5}Co_{0.2}Mn_{0.3}O₂ Cathode Material in Lithium Ion Batteries. *Adv. Energy Mater.* **2014**, *4* (1), 1300787. <https://doi.org/10.1002/aenm.201300787>.
- (5) Yang, X.-Q.; McBreen, J.; Yoon, W.-S.; Grey, C. P. Crystal Structure Changes of LiMn_{0.5}Ni_{0.5}O₂ Cathode Materials during Charge and Discharge Studied by Synchrotron Based in Situ XRD. *Electrochem. Commun.* **2002**, *4* (8), 649–654. [https://doi.org/10.1016/S1388-2481\(02\)00406-X](https://doi.org/10.1016/S1388-2481(02)00406-X).
- (6) Zhang, X.; Cheng, X.; Zhang, Q. Nanostructured Energy Materials for Electrochemical Energy Conversion and Storage: A Review. *J. Energy Chem.* **2016**, *25* (6), 967–984. <https://doi.org/10.1016/j.jechem.2016.11.003>.
- (7) Padhi, A. K.; Nanjundaswamy, K. S.; Goodenough, J. B. Phospho-olivines as Positive-Electrode Materials for Rechargeable Lithium Batteries. *J. Electrochem. Soc.* **1997**, *144* (4), 1188. <https://doi.org/10.1149/1.1837571>.
- (8) Zhang, W.-J. Structure and Performance of LiFePO₄ Cathode Materials: A Review. *J. Power Sources* **2011**, *196* (6), 2962–2970.
<https://doi.org/10.1016/j.jpowsour.2010.11.113>.
- (9) Liu, H.; Strobridge, F. C.; Borkiewicz, O. J.; Wiaderek, K. M.; Chapman, K. W.; Chupas, P. J.; Grey, C. P. Capturing Metastable Structures during High-Rate Cycling of LiFePO₄ Nanoparticle Electrodes. *Science* **2014**, *344* (6191), 1252817. <https://doi.org/10.1126/science.1252817>.

- (10) Zhang, X.; van Hulzen, M.; Singh, D. P.; Brownrigg, A.; Wright, J. P.; van Dijk, N. H.; Wagemaker, M. Rate-Induced Solubility and Suppression of the First-Order Phase Transition in Olivine LiFePO_4 . *Nano Lett.* **2014**, *14* (5), 2279–2285. <https://doi.org/10.1021/nl404285y>.
- (11) Hong, L.; Li, L.; Chen-Wiegart, Y.-K.; Wang, J.; Xiang, K.; Gan, L.; Li, W.; Meng, F.; Wang, F.; Wang, J.; Chiang, Y.-M.; Jin, S.; Tang, M. Two-Dimensional Lithium Diffusion Behavior and Probable Hybrid Phase Transformation Kinetics in Olivine Lithium Iron Phosphate. *Nat. Commun.* **2017**, *8* (1), 1–13. <https://doi.org/10.1038/s41467-017-01315-8>.
- (12) Laffont, L.; Delacourt, C.; Gibot, P.; Wu, M. Y.; Kooyman, P.; Masquelier, C.; Tarascon, J. M. Study of the $\text{LiFePO}_4/\text{FePO}_4$ Two-Phase System by High-Resolution Electron Energy Loss Spectroscopy. *Chem. Mater.* **2006**, *18* (23), 5520–5529. <https://doi.org/10.1021/cm0617182>.
- (13) Weichert, K.; Sigle, W.; van Aken, P. A.; Jamnik, J.; Zhu, C.; Amin, R.; Acartürk, T.; Starke, U.; Maier, J. Phase Boundary Propagation in Large LiFePO_4 Single Crystals on Delithiation. *J. Am. Chem. Soc.* **2012**, *134* (6), 2988–2992. <https://doi.org/10.1021/ja207124a>.
- (14) Morgan, D.; Ven, A. V. der; Ceder, G. Li Conductivity in Li_xMPO_4 (M = Mn, Fe, Co, Ni) Olivine Materials. *Electrochem. Solid-State Lett.* **2004**, *7* (2), A30–A32. <https://doi.org/10.1149/1.1633511>.
- (15) Wang, C.; Kasavajjula, U. S.; Arce, P. E. A Discharge Model for Phase Transformation Electrodes: Formulation, Experimental Validation, and Analysis. *J. Phys. Chem. C* **2007**, *111* (44), 16656–16663. <https://doi.org/10.1021/jp074490u>.
- (16) Liu, H.; Kazemiabnavi, S.; Grenier, A.; Vaughan, G.; Di Michiel, M.; Polzin, B. J.; Thornton, K.; Chapman, K. W.; Chupas, P. J. Quantifying Reaction and Rate Heterogeneity in Battery Electrodes in 3D through Operando X-Ray Diffraction Computed Tomography. *ACS Appl. Mater. Interfaces* **2019**, *11* (20), 18386–18394. <https://doi.org/10.1021/acsami.9b02173>.
- (17) Ohmer, N.; Fenk, B.; Samuelis, D.; Chen, C.-C.; Maier, J.; Weigand, M.; Goering, E.; Schütz, G. Phase Evolution in Single-Crystalline LiFePO_4 Followed by in Situ Scanning X-Ray Microscopy of a Micrometre-Sized Battery. *Nat. Commun.* **2015**, *6* (1), 1–7. <https://doi.org/10.1038/ncomms7045>.
- (18) Wang, J.; Chen-Wiegart, Y. K.; Wang, J. In Operando Tracking Phase Transformation Evolution of Lithium Iron Phosphate with Hard X-Ray Microscopy. *Nat. Commun.* **2014**, *5* (1), 1–10. <https://doi.org/10.1038/ncomms5570>.
- (19) Liu, Q.; Liu, Y.; Yang, F.; He, H.; Xiao, X.; Ren, Y.; Lu, W.; Stach, E.; Xie, J. Capacity Fading Mechanism of the Commercial 18650 LiFePO_4 -Based Lithium-Ion Batteries: An in Situ Time-Resolved High-Energy Synchrotron XRD Study. *ACS Appl. Mater. Interfaces* **2018**, *10* (5), 4622–4629. <https://doi.org/10.1021/acsami.7b13060>.
- (20) Mathiesen, J. K.; Johnsen, R. E.; Blennow, A. S.; Norby, P. Understanding the Structural Changes in Lithiated Graphite through High-Resolution Operando Powder X-Ray Diffraction. *Carbon* **2019**, *153*, 347–354. <https://doi.org/10.1016/j.carbon.2019.06.103>.
- (21) Sasaki, T.; Villevieille, C.; Takeuchi, Y.; Novák, P. Understanding Inhomogeneous Reactions in Li-Ion Batteries: Operando Synchrotron X-Ray Diffraction on Two-Layer Electrodes. *Adv. Sci.* **2015**, *2* (7), 1500083. <https://doi.org/10.1002/advs.201500083>.

- (22) Waluś, S.; Barchasz, C.; Bouchet, R.; Leprêtre, J.-C.; Colin, J.-F.; Martin, J.-F.; Elkaim, E.; Baecht, C.; Alloin, F. Lithium/Sulfur Batteries Upon Cycling: Structural Modifications and Species Quantification by In Situ and Operando X-Ray Diffraction Spectroscopy. *Adv. Energy Mater.* **2015**, *5* (16), 1500165.
<https://doi.org/10.1002/aenm.201500165>.
- (23) Herklotz, M.; Weiss, J.; Ahrens, E.; Yavuz, M.; Mereacre, L.; Kiziltas-Yavuz, N.; Dräger, C.; Ehrenberg, H.; Eckert, J.; Fauth, F.; Giebeler, L.; Knapp, M. A Novel High-Throughput Setup for in Situ Powder Diffraction on Coin Cell Batteries. *J. Appl. Crystallogr.* **2016**, *49* (1), 340–345. <https://doi.org/10.1107/S1600576715022165>.
- (24) Hess, M.; Sasaki, T.; Villevieille, C.; Novák, P. Combined *Operando* X-Ray Diffraction–Electrochemical Impedance Spectroscopy Detecting Solid Solution Reactions of LiFePO₄ in Batteries. *Nat. Commun.* **2015**, *6*, 8169. <https://doi.org/10.1038/ncomms9169>.
- (25) Orikasa, Y.; Maeda, T.; Koyama, Y.; Murayama, H.; Fukuda, K.; Tanida, H.; Arai, H.; Matsubara, E.; Uchimoto, Y.; Ogumi, Z. Transient Phase Change in Two Phase Reaction between LiFePO₄ and FePO₄ under Battery Operation. *Chem. Mater.* **2013**, *25* (7), 1032–1039. <https://doi.org/10.1021/cm303411t>.
- (26) Nikolowski, K.; Baecht, C.; Bramnik, N. N.; Ehrenberg, H. A Swagelok-Type in Situ Cell for Battery Investigations Using Synchrotron Radiation. *J. Appl. Crystallogr.* **2005**, *38* (5), 851–853. <https://doi.org/10.1107/S0021889805022302>.
- (27) Sottmann, J.; Homs-Regojo, R.; Wragg, D. S.; Fjellvåg, H.; Margadonna, S.; Emerich, H. Versatile Electrochemical Cell for Li/Na-Ion Batteries and High-Throughput Setup for Combined Operando X-Ray Diffraction and Absorption Spectroscopy. *J. Appl. Crystallogr.* **2016**, *49* (6), 1972–1981. <https://doi.org/10.1107/S160057671601428X>.
- (28) Cortes, F. J. Q.; Boebinger, M. G.; Xu, M.; Ulvestad, A.; McDowell, M. T. Operando Synchrotron Measurement of Strain Evolution in Individual Alloying Anode Particles within Lithium Batteries. *ACS Energy Lett.* **2018**, *3* (2), 349–355. <https://doi.org/10.1021/acseenergylett.7b01185>.
- (29) Ebner, M.; Marone, F.; Stampanoni, M.; Wood, V. Visualization and Quantification of Electrochemical and Mechanical Degradation in Li Ion Batteries. *Science* **2013**, *342* (6159), 716–720. <https://doi.org/10.1126/science.1241882>.
- (30) Liu, H.; Allan, P. K.; Borkiewicz, O. J.; Kurtz, C.; Grey, C. P.; Chapman, K. W.; Chupas, P. J. A Radially Accessible Tubular in Situ X-Ray Cell for Spatially Resolved Operando Scattering and Spectroscopic Studies of Electrochemical Energy Storage Devices. *J. Appl. Crystallogr.* **2016**, *49* (5), 1665–1673.
<https://doi.org/10.1107/S1600576716012632>.
- (31) Moroni, R.; Börner, M.; Zielke, L.; Schroeder, M.; Nowak, S.; Winter, M.; Manke, I.; Zengerle, R.; Thiele, S. Multi-Scale Correlative Tomography of a Li-Ion Battery Composite Cathode. *Sci. Rep.* **2016**, *6* (1), 1–9. <https://doi.org/10.1038/srep30109>.
- (32) Paz-Garcia, J. M.; Taiwo, O. O.; Tudisco, E.; Finegan, D. P.; Shearing, P. R.; Brett, D. J. L.; Hall, S. A. 4D Analysis of the Microstructural Evolution of Si-Based Electrodes during Lithiation: Time-Lapse X-Ray Imaging and Digital Volume Correlation. *J. Power Sources* **2016**, *320*, 196–203. <https://doi.org/10.1016/j.jpowsour.2016.04.076>.

- (33) Pietsch, P.; Hess, M.; Ludwig, W.; Eller, J.; Wood, V. Combining *Operando* Synchrotron X-Ray Tomographic Microscopy and Scanning X-Ray Diffraction to Study Lithium Ion Batteries. *Sci. Rep.* **2016**, *6*, 27994. <https://doi.org/10.1038/srep27994>.
- (34) Devaux, D.; Leduc, H.; Dumaz, P.; Lecuyer, M.; Deschamps, M.; Bouchet, R. Effect of Electrode and Electrolyte Thicknesses on All-Solid-State Battery Performance Analyzed With the Sand Equation. *Front. Energy Res.* **2020**, *7*. <https://doi.org/10.3389/fenrg.2019.00168>.
- (35) Kieffer, J.; Karkoulis, D. PyFAI, a Versatile Library for Azimuthal Regrouping. *J. Phys. Conf. Ser.* **2013**, *425* (20), 202012. <https://doi.org/10.1088/1742-6596/425/20/202012>.
- (36) Toby, B. H.; Von Dreele, R. B. GSAS-II: The Genesis of a Modern Open-Source All Purpose Crystallography Software Package. *J. Appl. Crystallogr.* **2013**, *46* (2), 544–549. <https://doi.org/10.1107/S0021889813003531>.
- (37) Finegan, D. P.; Vamvakeros, A.; Cao, L.; Tan, C.; Heenan, T. M. M.; Daemi, S. R.; Jacques, S. D. M.; Beale, A. M.; Di Michiel, M.; Smith, K.; Brett, D. J. L.; Shearing, P. R.; Ban, C. Spatially Resolving Lithiation in Silicon–Graphite Composite Electrodes via in Situ High-Energy X-Ray Diffraction Computed Tomography. *Nano Lett.* **2019**, *19* (6), 3811–3820. <https://doi.org/10.1021/acs.nanolett.9b00955>.
- (38) Zhong, X.; Yu, L.; Sun, J.; Zhang, Y.. Radiation Stability of PTFE Irradiated under Various Conditions. *Polym. Degrad. Stab.* **1993**, *39* (2), 187–191. [https://doi.org/10.1016/0141-3910\(93\)90094-Y](https://doi.org/10.1016/0141-3910(93)90094-Y).
- 39) Liu, J.; Kunz, M.; Chen, K.; Tamura, N.; Richardson T. Visualization of Charge Distribution in a Lithium Battery Electrode. *J. Phys. Chem. Lett.* **2010**, *1*(14), 2120–2123. <https://doi.org/10.1021/jz100634n>.
- 40) Strobridge, F.; Orvananos B.; Croft, M.; Yu H-C.; Robert, R.; Liu H.; Zhong, Z.; Connolley, T.; Drakopoulos M.; Katsuyo, T; Grey, C. Mapping the Inhomogeneous Electrochemical Reaction Through Porous LiFePO₄-Electrodes in a Standard Coin Cell Battery. *Chem. Mat.* **2015**, *27*, 2374–2386. <https://doi.org/10.1021/cm504317a>.
- 41) Orikasa, Y.; Gogyo, Y.; Yamashige, H.; Katayama, M.; Chen, K.; Mori, T.; Yamamoto, K.; Masese, T.; Inada, Y.; Ohta, T.; Siroma, Z.; Kato, S.; Kinoshita, H.; Arai, H.; Ogumi, Z.; Uchimoto, Y. Ionic Conduction in Lithium Ion Battery Composite Electrode Governs Cross-sectional Reaction Distribution. *Sci. Rep.* **2016**, *6*, 26382. <https://doi.org/10.1038/sr26382>.

List of Figure captions

Figure 1: Scheme of the experimental configuration used for the *operando* experiments.

Figure 2: **a)** Glass cell: picture, side-view sketch and X-ray diffraction pattern, **b)** Swagelok PTFE cell: picture, side-view sketch and X-ray diffraction pattern.

Figure 3: Synchrotron powder X-ray diffraction pattern and Rietveld refinement corresponding to the initial state of the battery assembly.

Figure 4: **a)** X-ray diffraction patterns collected at different heights of the battery assembly **b)** Phase distribution plots corresponding to Li (blue) and LFP (red) as a function of the battery assembly height.

Figure 5: **a)** XRD patterns of the cathode collected at the interface with SPE during charge and discharge. The main reflections of the LiFePO_4 and FePO_4 phases are indicated with orange and grey asterisks, respectively. **b)** Time as a function of the potential during electrochemical cycling.

Figure 6: **a)** Distribution of LFP and FP phases along the electrode height at different states of charge during charge and discharge, **b)** left: evolution of potential as a function of x in Li_xFePO_4 during the charge and discharge cycle, right: percentage of LFP phase during the charge and discharge cycle.

Figure 7: **a)** Phase distribution maps obtained from the reconstructed XRD patterns measured at the interface between the cathode and the SPE, **b)** reconstructed X-ray diffraction patterns corresponding to different radial positions of the XRD-CT slice.

Figures list

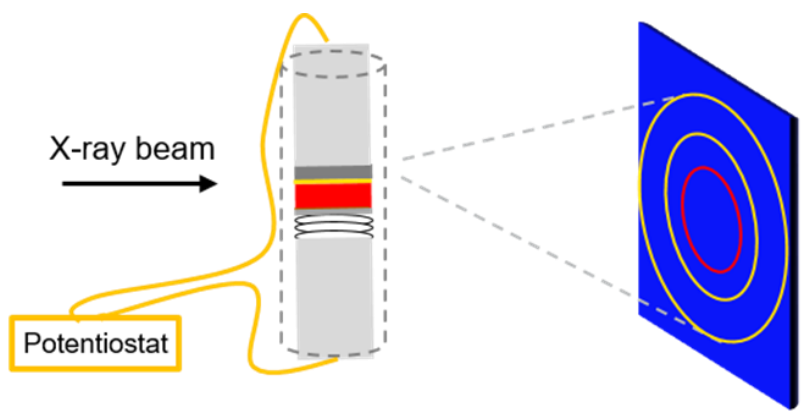


Figure 1: Scheme of the experimental configuration used for the *operando* experiments.

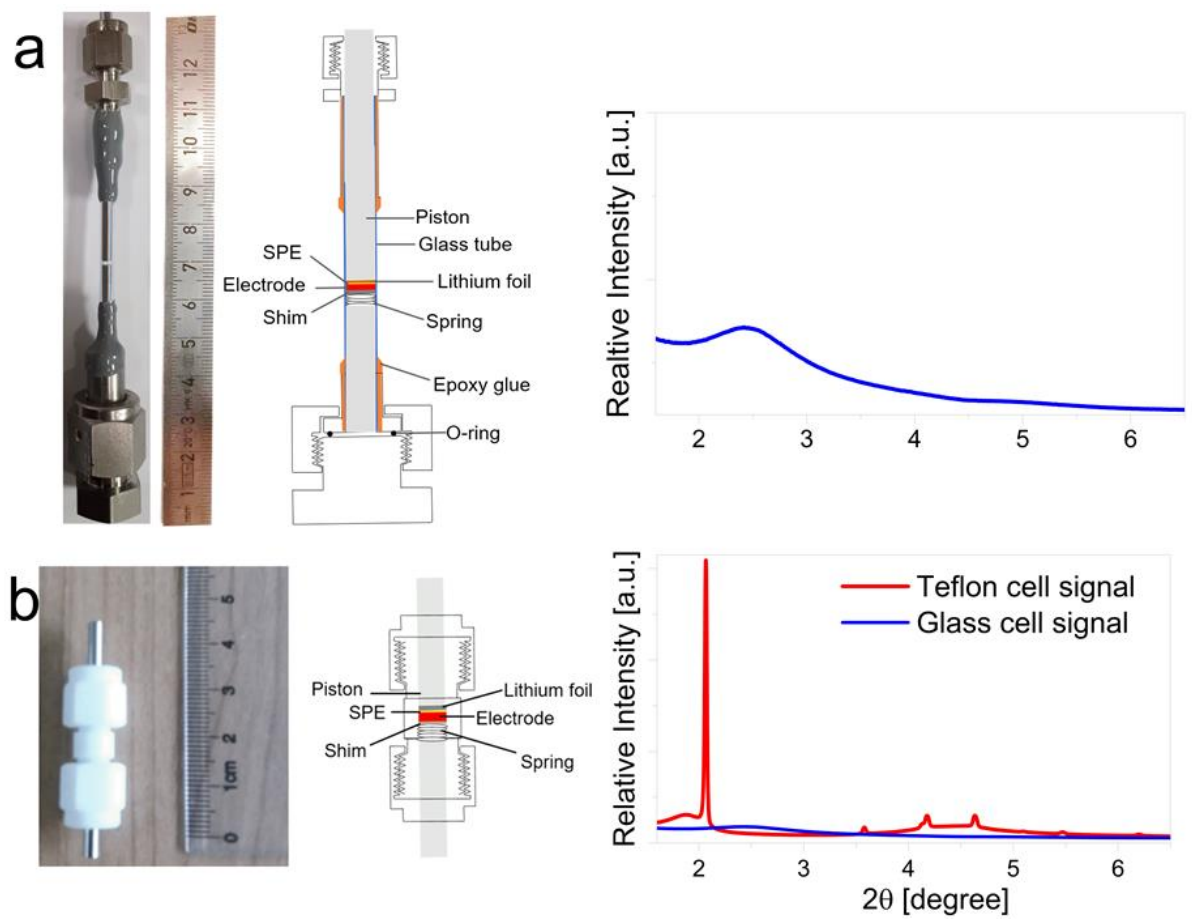


Figure 2: a) Glass cell: picture, side-view sketch and X-ray diffraction pattern, b) Swagelok PTFE cell: picture, side-view sketch and X-ray diffraction pattern.

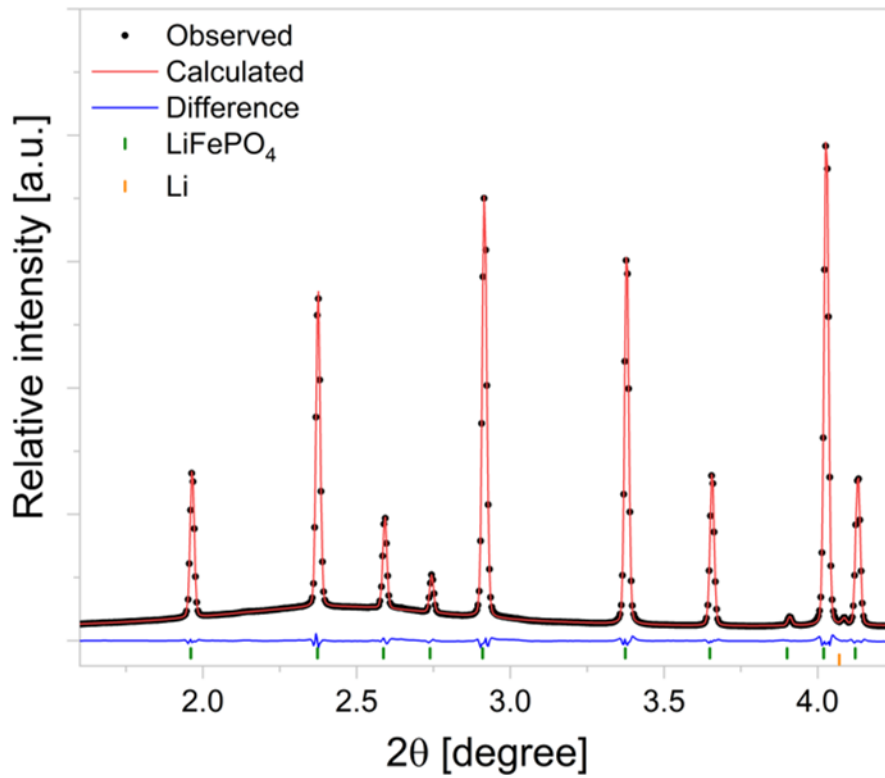


Figure 3: Synchrotron powder X-ray diffraction pattern and Rietveld refinement corresponding to the initial state of the battery assembly.

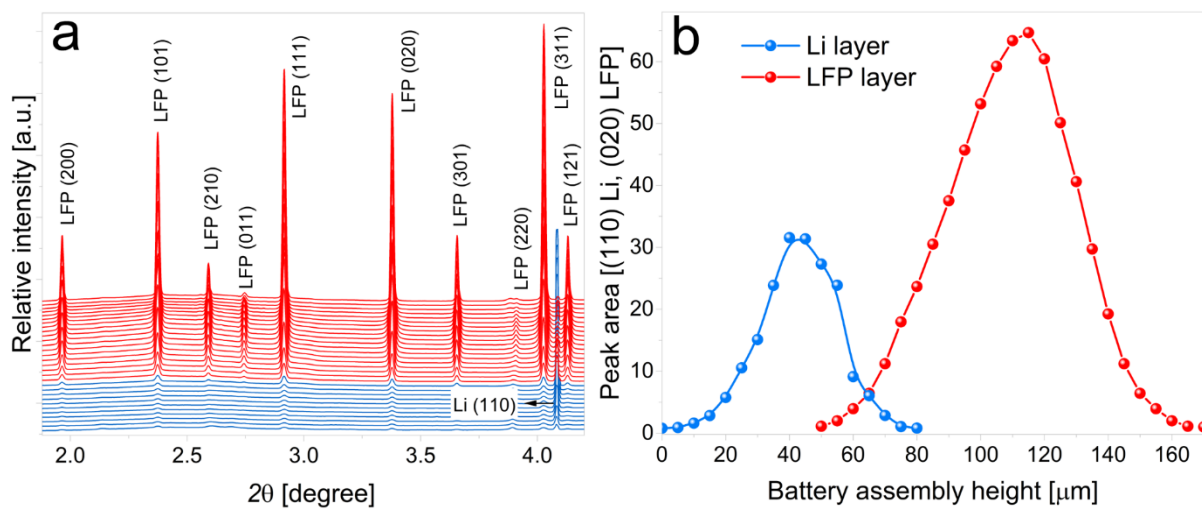


Figure 4: a) X-ray diffraction patterns collected at different heights of the battery assembly
 b) Phase distribution plots corresponding to Li (blue) and LFP (red) as a function of the battery assembly height.

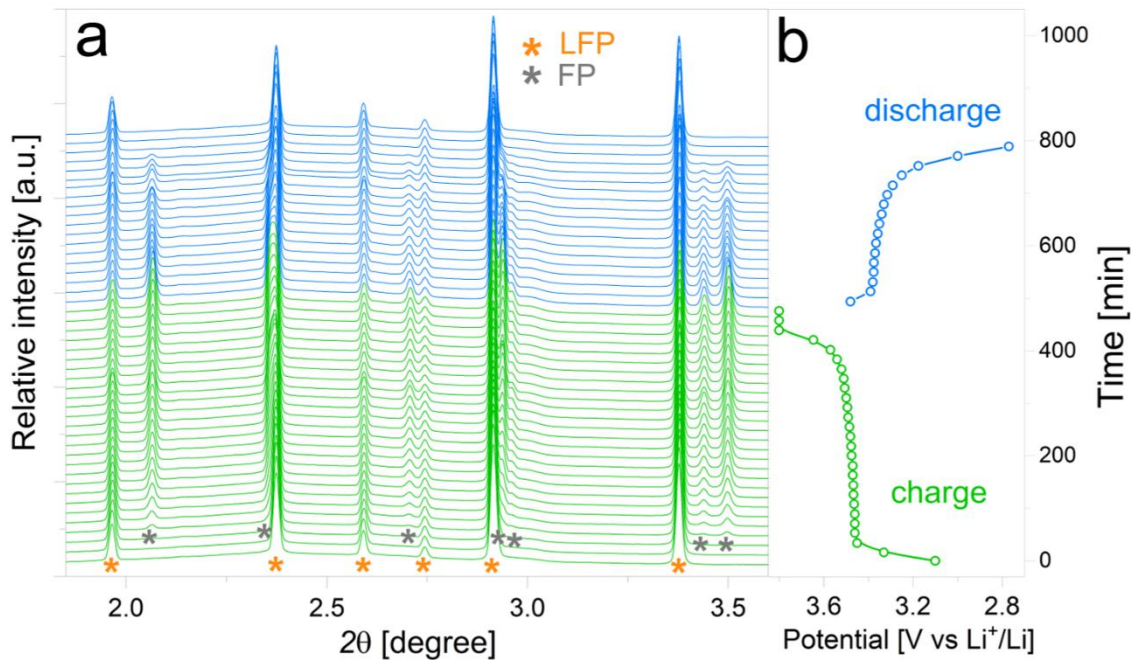


Figure 5: a) XRD patterns of the cathode collected at the interface with SPE during charge and discharge. The main reflections of the LiFePO₄ and FePO₄ phases are indicated with orange and grey asterisks, respectively. b) Time as a function of the potential during electrochemical cycling.

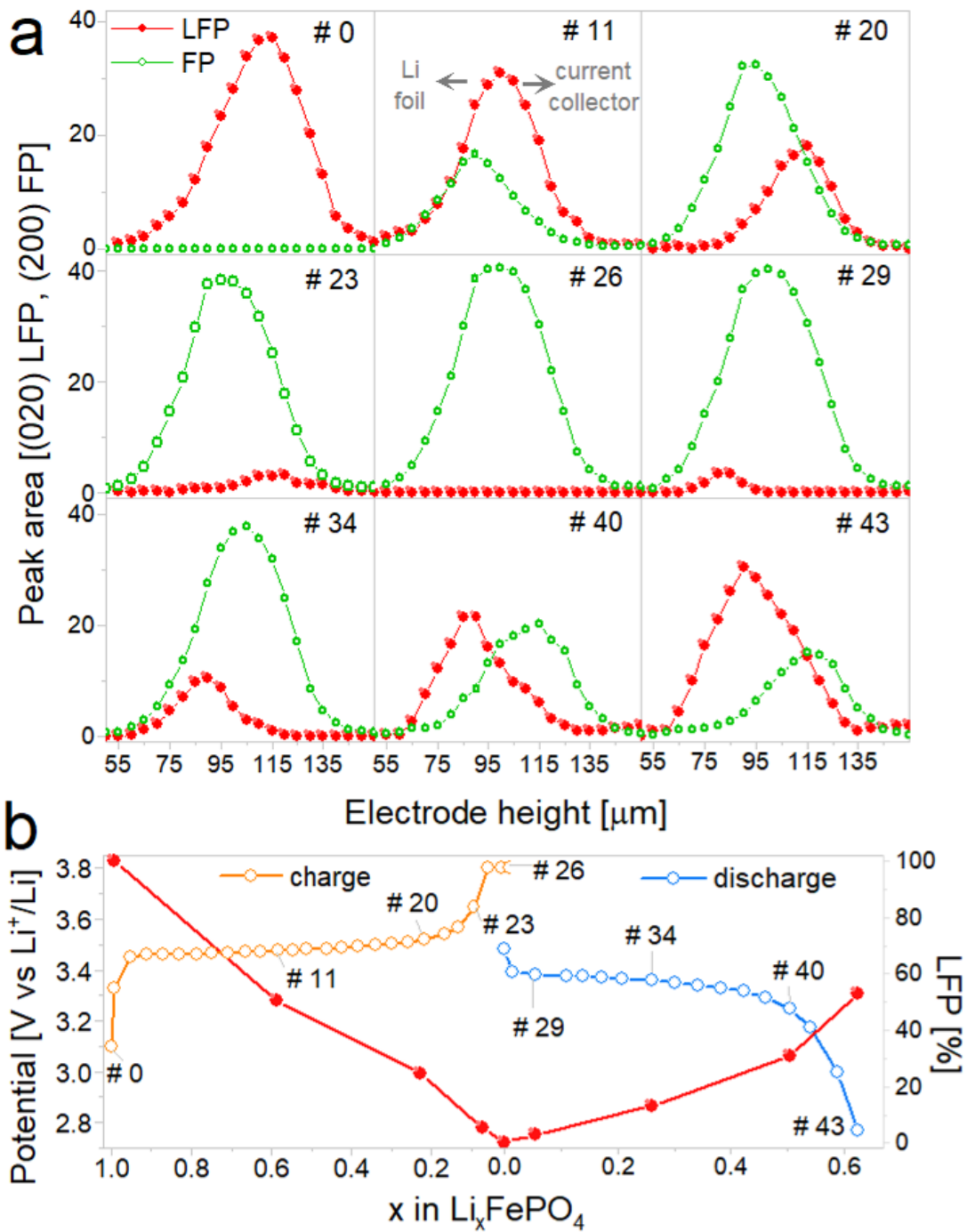


Figure 6: **a)** Distribution of LFP and FP phases along the electrode height at different states of charge during charge and discharge, **b)** left: evolution of potential as a function of x in Li_xFePO_4 during the charge and discharge cycle, right: percentage of LFP phase during the charge and discharge cycle.

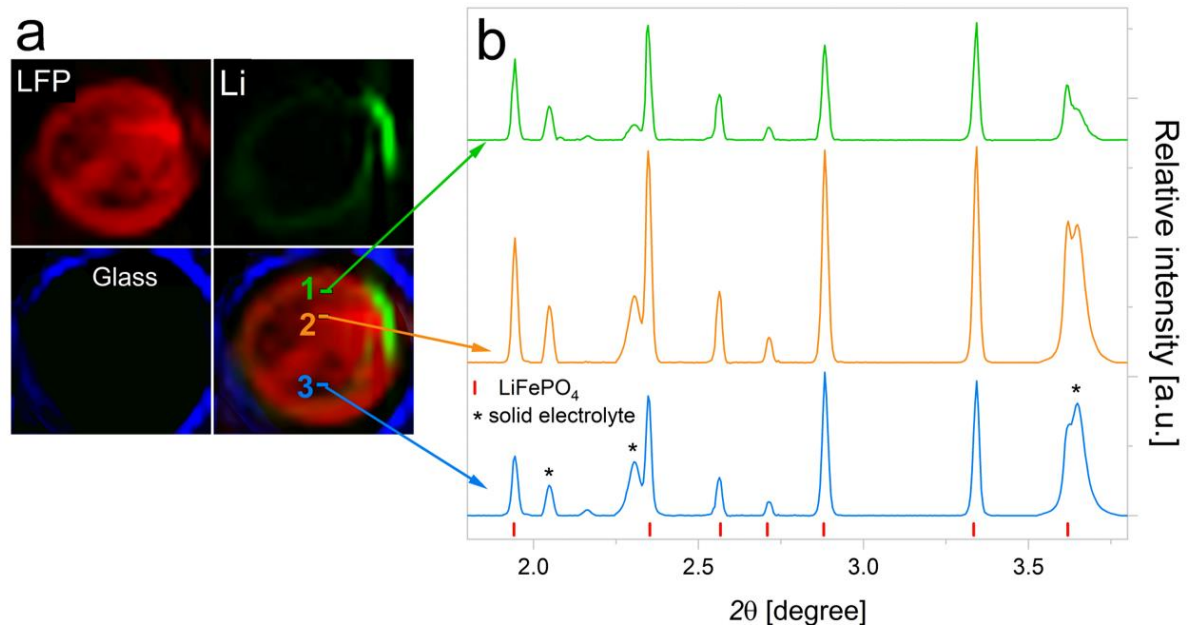


Figure 7: a) Phase distribution maps obtained from the reconstructed XRD patterns measured at the interface between the cathode and the SPE, b) reconstructed X-ray diffraction patterns corresponding to different radial positions of the XRD-CT slice.